Superpixel-Based Change Detection for GPR Time-Lapse Slices Using Fuzzy C-Means and the Markov Random Field Method

Yimin Zhou, Wallace Wai Lok Lai*, and Xiaolin Zhu

Ageing and complex underground utility infrastructure present a significant challenge for modern society, requiring long-term monitoring and maintenance to prevent economic and social costs associated with infrastructure degradation and failure. In this study, we proposed an unsupervised superpixel-based change-detection method using ground-penetrating radar time-lapse slices combining fuzzy C-means and the Markov random field model to investigate an invisible subsurface using time-series measurements. First, simple linear iterative clustering was applied to the difference image, which was generated using paired time-lapse images after intensity registration to create different scales superpixel maps. Then, fuzzy C-means clustering was used to generate superpixel-based change maps. Finally, the Markov random field model was used to integrate the information of adjacent neighbourhoods in three dimensions to iteratively refine the change map. We designed two underground cavities (one representing shallow local voids and the other representing voids near pipeline networks) to verify the capability and adaptability of the proposed method. The experimental results demonstrate the feasibility of the method, with F1-scores of 0.82, 0.69, 0.69, and 0.65 and kappa coefficients of 0.81, 0.69, 0.68, and 0.64. Our method represents a significant contribution to the field of GPR-based change detection and has the potential to improve the long-term monitoring and maintenance of complex underground utility infrastructure.

Keywords: Change detection, C-scan, Ground penetrating radar, Fuzzy c-means, Markov random field

1. Introduction

   High-density underground utilities are a crucial aspect of a modern metropolis, serving as the lifelines of a city's infrastructure. These utilities include water supply pipelines, sewer discharge systems, energy infrastructure, and telecommunication networks. However, the underground environment is becoming increasingly complex as cities develop (Broere, 2016). For instance, Hong Kong's roads may contain 47 km of underground pipelines for every 1 km of road. Ageing problems with underground pipelines are inevitable and can lead to severe disasters such as ground subsidence caused by void formation after pipes leak. Nonetheless, it is not practical to manually monitor underground utilities. Therefore, finding ways to sustainably maintain underground utilities non-invasively has become a crucial research topic. Ground-penetrating radar (GPR) technology is widely used to diagnose problems in underground utilities. A GPR transmitter emits electromagnetic waves underground, and a receiver records the signals reflected by the various host materials. Radargrams (B-scans), representing the vertical domain, and

time-lapse slices (or C-scans), representing the horizontal domain, provide 2D and 3D data(Jol, 2008). GPR technology offers rich information derived from 2D and 3D images, efficient data acquisition, and high spatial resolution(Annan, 2004).

Many studies have leveraged pattern recognition to identify underground objects such as voids, mines, and pipes based on one-shot B-scans(El-Mahallawy & Hashim, 2013; Feng et al., n.d.; Luo & Lai, 2020a; Milisavljeviã et al., 2003). However, one-shot observation does not provide the information necessary to understand the process by which a phenomenon or problem occurs. In contrast, change detection facilitates a dynamic analysis using multiple observation data, and it has been widely used in many fields, such as medical imaging and remote sensing(Rensink, 2002). Today, the evaluation of disease severity and changes over time using medical images is an important and routine task(Li et al., 2020). Similarly, timely and accurate change detection of Earth's surface features provides the foundation for a better understanding of the relationships and interactions between human and natural phenomena and better management of resources(Lu et al., 2004).

In the past two decades, various change-detection methods for images have been proposed. These methods can be classified according to their scale, including pixel-level(Chi et al., 2007; Rokni et al., 2015; Stow, 1999), object-level(Desclée et al., 2006; Simanjuntak et al., 2019; Walter, 2004), feature-level(Lv et al., 2018; Seo et al., 2022; Zhang & Shi, 2020), and hybrid-level(Hussain et al., 2013) methods. In the GPR field, it has been suggested that a single measurement is not reliable for determining small changes(Luo & Lai, 2020b). Establishing a time series of time-lapse GPR C-scans is one way to identify potential subsurface defects. Through comparison with the baseline, potential defects can be easily identified from GPR C-scan images. This approach facilitates subsurface surveys on a city scale: if only changed areas need to be inspected, the maintenance workload will be decreased significantly. However, change detection using GPR time-lapse slices has seldom been researched(Luo & Lai, 2020b).

Unlike B-scans, C-scans provide straightforward horizontal representations of the underground, enabling the detection of changes in large regions. C-scans do not require the survey area to be measured using the same surveying traverses. In addition, it is time- and labor-intensive to manipulate change detection in massive B-scans. Thus, a fast and robust method for change detection from images is desired to extract dissimilarities from time-lapse GPR C-scans. However, change detection using GPR C-scans is challenging. First, image registration is necessary for multiple measurements. Received GPR signals are the convolutions of the propagation of electromagnetic waves, and are a mixture of reflection, refraction, scattering, and reverberation. Temporal GPR data are affected by various factors, including moisture conditions, temperature, and antenna energy, which can be regarded as noise and must be mitigated by image registration. Second, pattern recognition must adapt to C-scans because time-lapse C-scans are generated by interpolation, which represents the normalised reflection intensity. Compressing the vertical information to a horizontal intensity distribution results in the loss of patterns of signal proportion. In addition, interpolated images contain artificial uncertainty from sample point distributions and parameter settings. The last challenge is the incorporation of the neighborhood's

information. C-scans compress the continuous underground space into slices, but changes in the vertical direction are hidden in adjacent slices. Integrating this adjacent three-dimensional information is important for the change detection task.

To address these challenges, this study proposed an unsupervised superpixel-based change detection method. First, an intensity registration module was applied to adjust a pair of C-scans. Secondly, superpixels were segmented from image differences and used as the basic unit along with the whole change detection workflow to reduce the effect of noise and filter out small changes. Then, fuzzy c-means clustering (FCM) and Markov random field (MRF) algorithm were adapted to C-scans change detection. Specifically, we proposed the use of a fuzzy C-means clustering algorithm to classify superpixel-based differences in images generated by a simple linear iterative clustering method into initial change maps. Additionally, we utilized the probability of superpixels to represent the soft relationship, as opposed to the traditional hard label (changed or unchanged). The fuzzy relationship was implemented appropriately when measuring the spatial attraction components of the Markov random field model. The developed MRF model with spectral and spatial components not only involves intensity information but also takes the adjacent neighbors in all three dimensions into consideration.

2. Methodology

Fig. 1 shows the flowchart of our proposed superpixel-based change detection method combining FCM and MRF. The method encompasses two main processes: time-series C-scan generation and C-scan change detection.
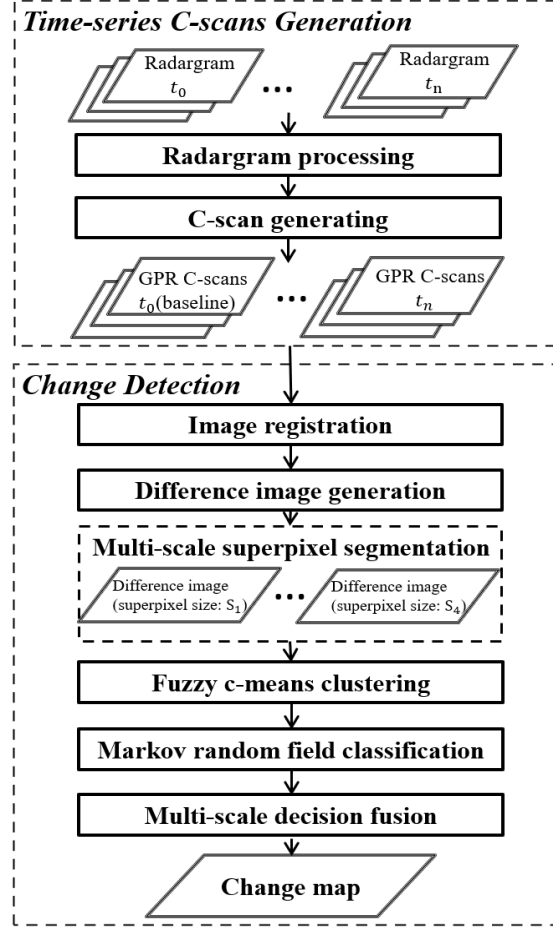
Fig. 1. Workflow of the proposed superpixel-based change detection method

A. Time-Series C-Scan Generation

   Radargrams collected at two different times were processed by basic 2D signal processing functions. These functions include de-wow to remove low-frequency noise, direct-current shift to correct the shift in the waveform, static correction to adjust time zero, range gain for consistent amplitude contrast, bandpass, background removal, and migration(Joll, 2009). Subsequently, C-scans were generated using GPRSlice, a third-party commercial GPR imaging software package(Goodman, 2004). The B-scans were stacked into C-scans based on a predesigned survey grid. Thus, each GPR signal was registered using local coordinates, and the profile spacing was less than 3λ (λ refers to the wavelength of the electromagnetic (EM) wave) following the 3D GPR imaging criteria in Fig.2 (Luo et al., 2019). To generate the C-scans, we specified three main parameters: profile spacing (PS), slice thickness (ST), and search radius (SR), and used bi-linear interpolation for filling in any missing data points. The profile spacing was set to 10cm less than 3λ, where λ is the wavelength of the GPR signal, to balance the measurement effort and data resolution. Our primary goal in this study was to explore the feasibility of using C-scans for change detection tasks based on data collected using the same procedures. The laboratory environment in which the study was conducted allowed for a relatively dense profile spacing. We set the slice thickness to 0.9λ (15cm) for sufficient resolution in the vertical direction. To interpolate

missing data points, we used bi-linear interpolation with a search radius of 0.9λ (15cm), which is recommended to be larger than the profile spacing to involve information from adjacent survey lines.
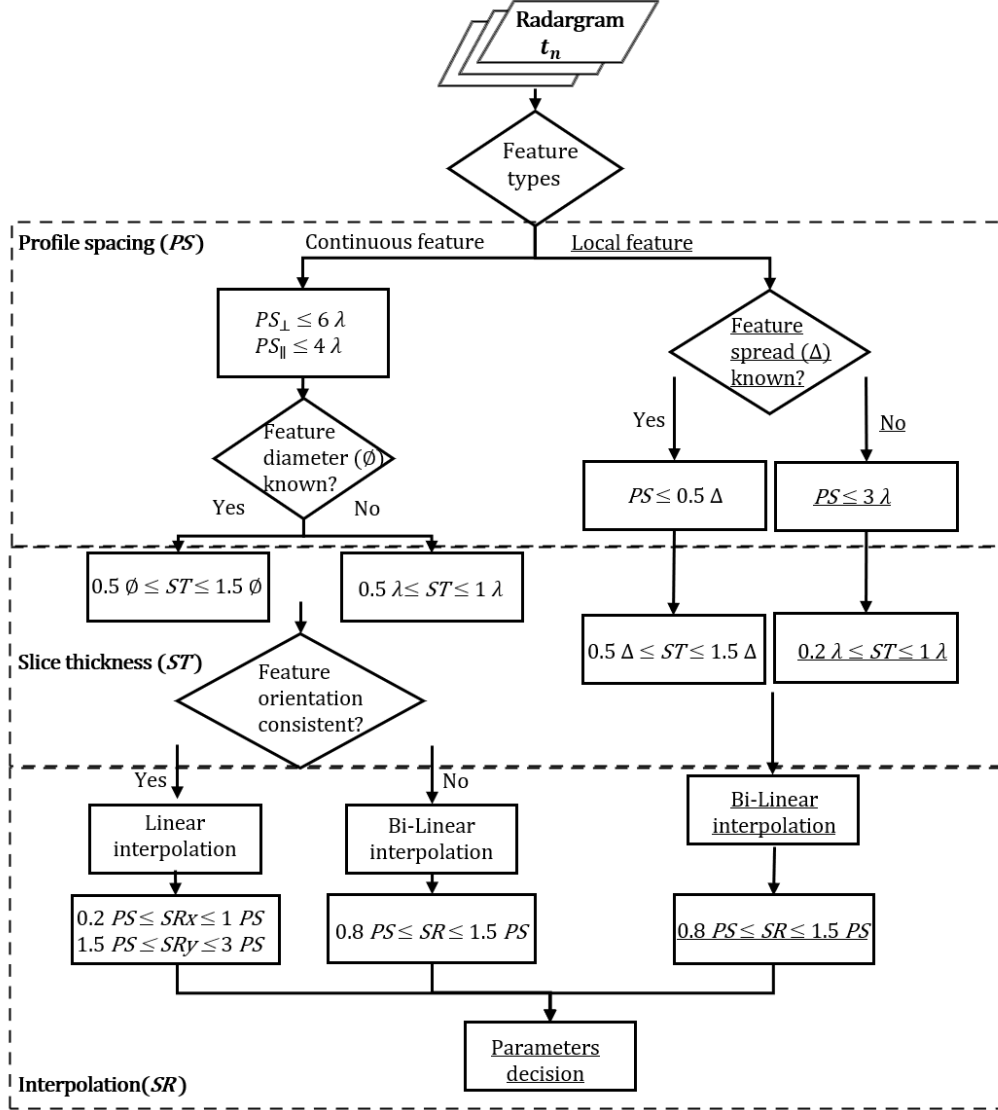
Fig. 2. 3D GPR imaging workflow. *PS*: profile spacing; *ST*: slice thickness; *SR*: search radius; λ: wavelength of the EM wave propagation underground (The underlined marks in the figure denote the parameter choices used in our method).

B. C-scan Change Detection

1). C-scan Image Registration

The reflected signal and locations in ground-penetrating radar (GPR) surveys are subject to multiple factors that may introduce variations in the GPR signals collected over time. To address this issue, image registration is typically employed as the first step in adjusting a pair of C-scans to a similar intensity range. Intensity-based image registration estimates the transformation that aligns target images to

baseline images based on their intensity values. This task can be formulated as an optimization problem with four primary components: transformation type, similarity metric function, interpolator, and optimizer. In the present study, we implemented affine transformation, correlation, linear interpolation, and gradient descent optimization in C-scan intensity registration. The moving image is transformed to match the fixed image in the registration procedure, and the optimizer adjusts the affine transformation matrix iteratively based on the gradient descent direction until the correlation between the moving image and the fixed image meets the threshold. Linear interpolation converts a discrete set of intensity values at grid locations to a continuous domain, which is required for the transformation. To achieve C-scan image intensity registration, we employed the SimpleITK registration framework (Lowekamp et al., 2013), which provides stable performance and can be used to effectively design each component using multiple programming language packages.

2). Difference Image (DI) Generation and Multiscale Superpixel Segmentation

After utilizing the C-scan image registration module, the pair of C-scans were corrected into similar intensity ranges. A superpixel is a homogeneous block that shares the same intensity value within a certain distance. The superpixel was used as the basic processing unit in this study for two reasons: it reduces local random noise and it upscales the basic unit to keep our focus on major change rather than over-detailed branches. To obtain the superpixel-based difference image(DI), contrast limited adaptive histogram equalization (CLAHE) and a simple linear iterative clustering (SLIC) algorithm were applied to normalize and segment the homogeneous block(Achanta et al., 2012; Reza, 2004). The DI is calculated using the following formula:

$$S_D^a = \left| CLAHE\left(S_{t_x}^a\right) - CLAHE\left(S_{t_0}^a\right) \right| \qquad (1)$$

Where, $S_{t_0}^a$ and $S_{t_x}^a$ are a^{th} registered C-scans generated by the data acquired in t_0 and t_x, where a is the index of the C-scans ($1 < a < A$). S_D^a denotes the DI of a pair of ath registered C-scans after CLAHE enhancement.

In this study, the SLIC method was used to segment DI into superpixel-based DI considering each superpixel as a homogeneous block with similar image features. Specifically, SLIC adapts k-means clustering with limited search regions to generate superpixels iteratively following intensity and spatial proximity. The intensity and spatial proximity with intensity distance d_I and spatial distance d_S between two pixels i, j is written as follows:

$$\begin{cases} D = \sqrt{\left(\dfrac{d_I}{M_I}\right)^2 + \left(\dfrac{d_S}{M_S}\right)^2 m} \\ M_S = S = \sqrt{N_P/K} \\ M_I = I_{max} - I_{min} \end{cases} \qquad (2)$$

$$\begin{cases} d_I = \sqrt{(I_i - I_j)^2} \\ d_S = \sqrt{(x_i - x_j)^2 + (y_i - y_j)^2} \end{cases} \qquad (3)$$

Where distance D was calculated by d_I and d_S, and M_I and M_S represent the maximum intensity distance and maximum spatial distance, respectively. m is a relative factor to weigh the intensity and spatial similarity. $I_i, x_i,$ and y_i refer to the intensity value and the position coordinates of the ith pixel, respectively. The maximum spatial distance within a given cluster is related to the sample interval, $M_S = S = \sqrt{N_P/K}$, in which N_P is the number of pixels in a whole C-scan and K is the number of superpixels. The maximum spectral distance is the difference between the maximum and minimum intensity values of the pixels in the given cluster. The scale has been stressed as a key parameter for discrimination(Inglacla & Mercier, 2007) between change and unchanged areas. A multiscale strategy is implemented to reduce misdetection or detections by generating difference images with varying sizes of superpixels $S_n = \left\{ \frac{S}{n} \middle| n = 1,2,3,4 \right\}$.

The superpixel-based DI was generated using the previous equations; hence, superpixels of the DI were used instead of pixels as the basic processing unit for the rest of the modules. Given a set with K superpixels, $R_a^{S_n} = \left\{ r_{k_a}^{S_n} \middle| k = 1 \dots K, n = 1,2,3,4 \right\}$ represents a superpixel-based DI generated by pair of ath C-scans with superpixel size S_n, where $I_{r_{k_a}^{S_n}}$ is the intensity of the superpixel $r_{k_a}^{S_n}$ and the intensity of the superpixel was obtained by the mean value of the pixel-based DI within the cluster region. Fig. 3. provides an example of our superpixel segmentation approach, The 'target size', a user-specified parameter, sets the size of level-1 superpixels. The 'target size' is meticulously tailored to correspond to the scale of the features targeted for detection and analysis. Consequently, a larger 'target size' may potentially underemphasize minute variations within the image, while a smaller 'target size' may accentuate these nuances. Level-2 superpixels are one-fourth of the target size, while level-3 and level-4 superpixels are one-ninth and one-sixteenth of the target size, respectively.
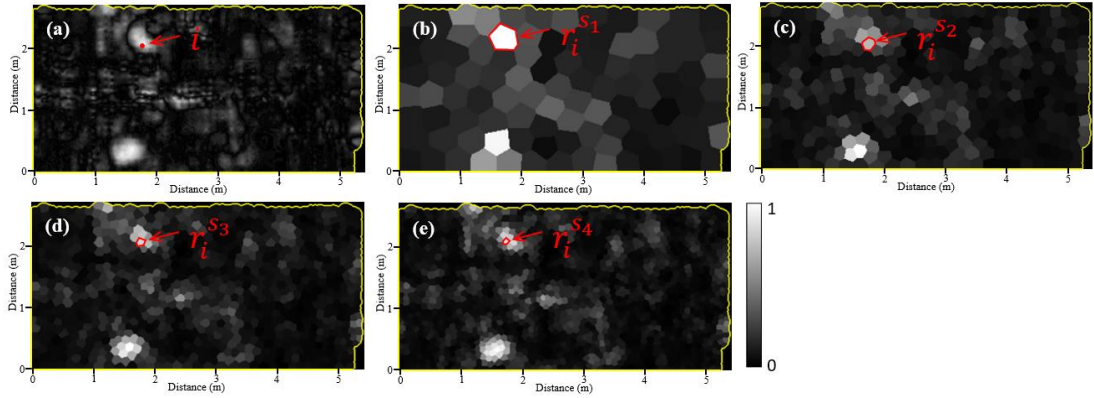
Fig. 3. Illustrations of pixel-based DI map and multiscale DI maps (a) pixel-based DI map; superpixel-based DI maps: (b) level-1; (c) level-2; (d) level-3; (e) level-4.

3). Fuzzy C-Means Clustering

Fuzzy C-means clustering (FCM) is a widely used clustering algorithm (Bezdek, 1984). The change detection task can be regarded as a binary classification, and the clustering algorithm divides the DI into changed and unchanged regions. FCM, combined with fuzzy set theory, uses the possibility of change occurrence instead of a hard boundary between changed and unchanged states, as depicted in Fig. 4.
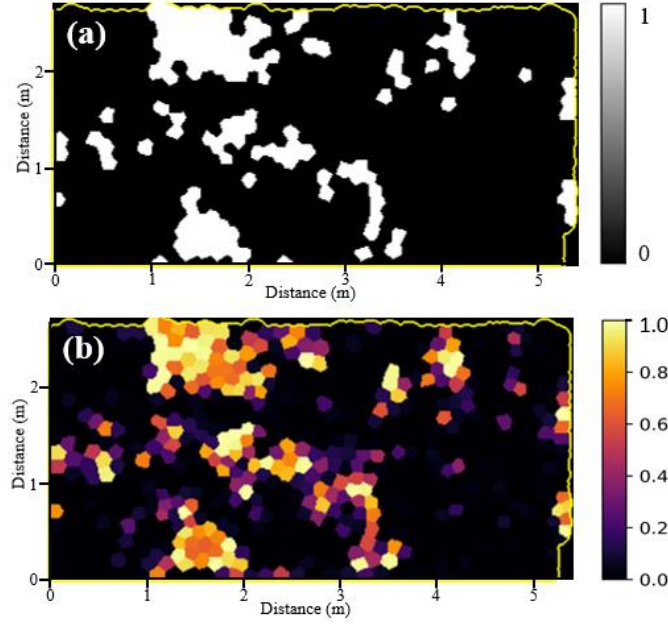
Fig. 4. Soft label clustering illustration: (a) hard classification: 0 indicates unchanged and 1 indicates changed; (b) soft classification: the values refer to the probability of change.

Given C classes, the DI of ath C-scan with level-n superpixel size is represented by $R_a^{S_n}$. For simplicity and clarity, they are represented by $R = \{r_k \mid k = 1 \ldots K\}$ in this sub-section. FCM aims to minimize the objective function by assigning each r_k to different classes and corresponding memberships iteratively, as follows:

$$J = \sum_{k=1}^{K} \sum_{c=1}^{C} u_{kc}{}^q \parallel I_{r_k} - v_c \parallel^2 \tag{4}$$

$$\begin{cases} u_{kc} = \sum_{h=1}^{C} (\dfrac{\parallel I_{r_k} - v_c \parallel}{\parallel I_{r_k} - v_h \parallel})^2 \\[2mm] v_c = \dfrac{\sum_{k=1}^{K} u_{kc}{}^q \cdot I_{r_k}}{\sum_{k=1}^{K} u_{kc}{}^q} \end{cases} \tag{5}$$

Where K is the number of superpixels, C is the number of classes and equals 2, q is the weighting exponent of FCM and equals 2, u_{kc} is the partition of the kth superpixel in the cluster C of the R, and v_c is the cth cluster center. We randomly assigned initial membership and cluster centers. To ensure convergence of the algorithm, we set two termination conditions. The first was based on the convergence of the objective function. We terminated the algorithm when the decrease in the objective function between two consecutive iterations was below a threshold of 0.001. The second termination condition was the maximum iteration number, which we set to 500.

After clustering, the possibility of each superpixel belonging to the changed cluster was normalized to [0,1], according to DI values. In addition, the initial single C-scan change map was generated by assigning the membership of each superpixel.

4). Markov Random Field for Multi-Slice Change Detection and Multiscale decision fusion

C-scans are present underground through a series of horizontal images based on depth range. Although changes may exhibit clear patterns, vertical information should also be considered. To obtain effective neighborhood information in three dimensions, the superpixel neighborhoods were defined as an adjacent set $R_{a^j}^{S_n} = \left\{ r_{k_{a^j}}^{S_n} \mid j = 1 \dots J \right\}$, as illustrated in Fig.5.
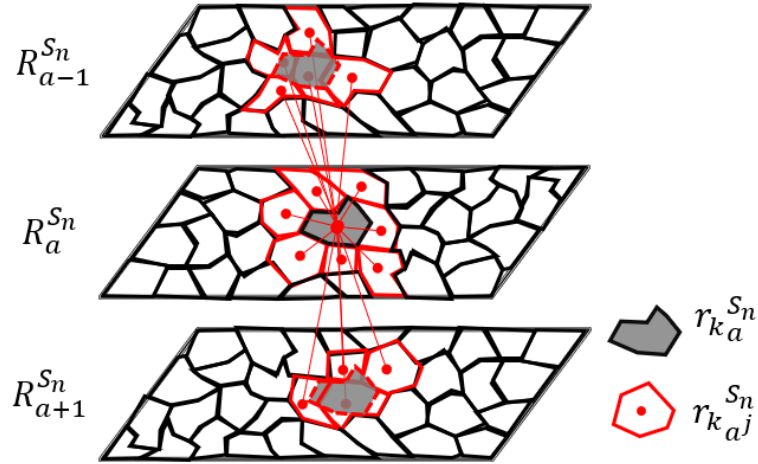
Fig. 5. Superpixel-adjacent neighborhoods in three dimensions.

Suppose that $L = \left\{ l_{r_{k_a}^{S_n}} \mid k = 1 \dots K, n = 1,2,3,4 \right\}$ represents the label sets of the superpixels, in which $l_{r_{k_a}^{S_n}}$ is the label of superpixel $r_{k_a}^{S_n}$, which is equal to 0 or 1 (changed or unchanged, respectively). Let $X = \left\{ r_{k_a}^{S_n} \mid k = 1 \dots K, n = 1,2,3,4 \right\}$ denote the C-scan set composed of K superpixels. The maximum a posteriori (MAP) estimation is used to obtain the labels of a superpixel, namely

$$L = arg \max\{P(L)P(X|L)\} \qquad (6)$$

where $P(X|L)$ is the joint conditional probability distribution of the superpixel set X and $P(L)$ is the prior probability of the class label L. Under the MRF approach, the MAP is equivalent to maximizing the following energy function U_{MRF} with the spectral and spatial components from multi-scaled DI images:

$$U_{MRF} = \sum_{n=1}^{N} U_{MRF}^{S_n} \qquad n = 1,2,3,4 \qquad (7)$$

$$U_{MRF}^{S_n} = U_{spectral}^{S_n} + \beta * U_{spatial}^{S_n} \qquad (8)$$

$$\begin{cases} U_{spectral}^{S_n}(r_{k_a}^{S_n}) = \dfrac{1}{2} ln\left(2\pi {\sigma_a^{S_n}}_l^2\right) + \dfrac{1}{2}\left(I_{r_{k_a}^{S_n}} - {\mu_a^{S_n}}_l\right)^2 ({\sigma_a^{S_n}}_l^2)^{-1} \\[2ex] U_{spatial}^{S_n}(r_{k_a}^{S_n}) = \displaystyle\sum_{j=1}^{J} I\left(l_{r_{k_a}^{S_n}}, l_{r_{k_{a^j}}^{S_n}}\right) \end{cases} \qquad (9)$$

where μ_l and σ_l are the mean and variance intensity of superpixels belonging to the label l, $I_{r_k^{S_n}}$ is the intensity of superpixel $r_k^{S_n}$, and β is the relative weight parameter between spectral energy and spatial energy.

The spatial energy term can be described in detail as follows:

$$I\left(l_{r_{k_a}^{S_n}}, l_{r_{k_{a^j}}^{S_n}}\right) = \begin{cases} w_{kj}, & l_{r_{k_a}^{S_n}} = l_{r_{k_{a^j}}^{S_n}} = 1 \\[1.5ex] 0, & l_{r_{k_a}^{S_n}} \neq l_{r_{k_{a^j}}^{S_n}} \end{cases} \qquad (10)$$

$$w_{kj} = l(f_k) \times l(f_k^j) \times \dfrac{1}{R(r_{k_a}^{S_n}, r_{k_{a^j}}^{S_n})} \qquad (11)$$

$$R\left(r_{k_a}^{S_n}, r_{k_{a^j}}^{S_n}\right) = \begin{cases} \sqrt{(x_{r_{k_a}^{S_n}} - x_{r_{k_{a^j}}^{S_n}})^2 + (y_{r_{k_a}^{S_n}} - y_{r_{k_{a^j}}^{S_n}})^2}, & A(r_{k_a}^{S_n}) = A\left(r_{k_{a^j}}^{S_n}\right) \\[2ex] \sqrt{(x_{r_{k_a}^{S_n}} - x_{r_{k_{a^j}}^{S_n}})^2 + (y_{r_{k_a}^{S_n}} - y_{r_{k_{a^j}}^{S_n}})^2 + ST^2}, & A(r_{k_a}^{S_n}) \neq A\left(r_{k_{a^j}}^{S_n}\right) \end{cases} \qquad (12)$$

Where, w_{kj} denotes the spatial attraction between $r_{k_a}^{S_n}$ and its adjacent neighborhoods $r_{k_{a^j}}^{S_n}$. $l(f_k)$ are the members belonging to class l of the superpixel. $r_{k_a}^{S_n}$ from $u_{a}^{S_n}{}_{kc}$ of FCM results, $R(r_{k_a}^{S_n}, r_{k_{a^j}}^{S_n})$ denotes the Euclidean distance between the centroids of superpixel $r_{k_a}^{S_n}$ and $r_{k_{a^j}}^{S_n}$. Equation (12) is to calculate the Euclidean, taking into account whether they belong to the same depth or not. $A(r_{k_a}^{S_n})$ denotes the index of the C-scan which $r_{k_a}^{S_n}$ is belonging to, and ST refers to the slicing thickness from the C-scan generation function dealing with $r_{k_a}^{S_n}$ and $r_{k_{a^j}}^{S_n}$ belonging to different C-scans. The iteration condition model (ICM) was used in this study to solve equation (7)(Zhu & Liu,

2014). The final change map is obtained when the iterative termination condition is met or the maximum iteration number is reached.

C. Accuracy Assessment

To quantify the accuracy of the proposed superpixel-based change detection method in the designed situations. Several commonly used indices, TP (true positive), FP (false positive), TN (true negative), FN (false negative), F1-score, and the kappa coefficient, were selected to estimate the results. TP means the correctly detected changed pixels that contain voids, FP means incorrectly detected changed pixels that don't contain voids, TN means correctly detected unchanged pixels that don't contain voids and FN means incorrectly detected unchanged pixels that contain voids. The F1-score and kappa coefficient were calculated as follows:

$$F1 - score = \frac{2 * (precision * recall)}{(precision + recall)} \qquad (13)$$

$$\begin{cases} precision = \dfrac{TP}{TP + FP} \\ recall = \dfrac{TP}{TP + FN} \end{cases} \qquad (14)$$

$$Kappa\ coefficient = \frac{2 \times (TP \times TN - FN \times FP)}{(TP + FP) \times (FP + TN) + (TP + FN) \times (FN + TN)} \ (15)$$

3. Experiment

Subsurface hazards can emerge suddenly and unexpectedly, leading to serious damage and safety risks, such as road collapses. Despite the potential benefits of GPR-image-based disaster monitoring, the lack of validation data poses a significant challenge for method development. To overcome this limitation, it is essential to have an experimental site that can simulate various underground conditions. The utility laboratory at The Hong Kong Polytechnic University provides a manipulable test bench, which allows for the observation of time-series data under controlled underground conditions. As depicted in Fig. 6. (a) and (b), the entire experimental site (3 m × 5 m) has a removable cover. It also includes pipes of different materials and manholes in various orientations, making up a complex underground scenario. All utilities were buried under soil with covers on top, allowing the creation of diverse underground situations. Fig. 6. (b) also shows the GPR antenna (IDS Hi-Mod) used in this experiment following the grid shown in Fig. 6. (c) with orthogonal grid cells at 10 cm intervals. Different kinds of targets, including spherical fitness balls and peanut-shaped fitness balls were put into the soil to simulate different shapes of underground cavities; see Fig. 6. (d), (e), and (f).
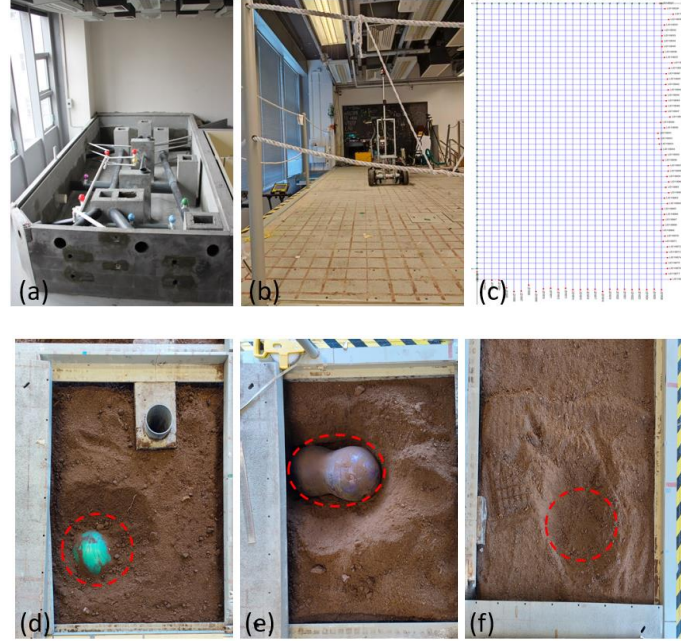
Fig. 6. Photos of the experiment site and targets. (a) the pipe and manhole distribution at the test site; (b) the test site and the IDS hi-mod antenna; (c) surveying grid of the test site; (d) a buried spherical fitness ball; (e) a buried peanut-shaped ball; (f) a void between pavement and soil.
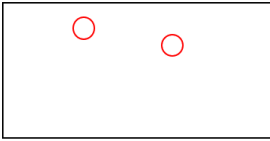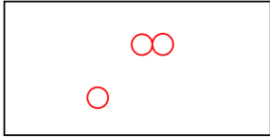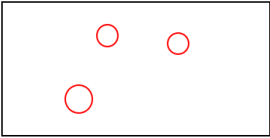
In this study, we designed four scenarios to evaluate the performance of the GPR system in detecting underground voids, as summarized in Table 1. We employed an auto-tracked position system to track survey lines on an orthogonal grid, collecting data using a 600 MHz antenna at 1 cm sampling intervals. The experimental design aimed to simulate the formation of underground voids in practical situations. Specifically, we placed the buried balls near the pipes, mimicking the scenario where water leaks from pipes and causes soil erosion to form voids. We also designed an isolated void to replicate the situation where the heavy pressure of the road results in soil loss and cavity formation. To verify the boundary of effective detection, balls of various sizes were utilized. Additionally, we used peanut-shaped balls to create voids with multiple centers. To imitate the time-series environment of void formation and remediation, each of the four scenarios was measured twice: once with voids present (void case) and once with the voids excavated and filled with soil (no void case).

Table 1

Distribution and sizes of buried targets of the Four Scenarios

Dataset	Distribution of the buried balls	Size of buried balls
Scenario A	Depth: 30cm	Shallow local voids (diameter: 36cm,36cm) marked as Ⓢ; One ball (diameter: 28cm) One peanut shape ball

|		at(diameter: 28cm in both sides)
Scenario B	Depth: 45cm	Two balls (diameter: 28cm,28cm)
Scenario C	Depth: 45cm	One ball (diameter: 28cm); One peanut shape ball (diameter: 28cm in both sides)
Scenario D	Depth:60cm	Three balls (diameter: 36cm,28cm,28cm)

4. Result and discussion

A. *Details and noise*

Preserving image details and providing noise immunity are two major objectives of the designed methods. The pre-processing CLAHE function enhances the image details, while the superpixel segmentation and MRF modules contribute to noise resistance. Moreover, a multi-scale strategy is implemented to balance detail preservation and noise reduction.

A common phenomenon in change detection is that the changed areas often constitute a small fraction of the entire survey site, resulting in a large concentration of pixels with DI values concentrated around zero, as evident from the green histograms in Fig. 7. (c) and (f). In such instances, image enhancement functions are necessary to improve the quality of the raw images for better analysis. The pre-processing CLAHE function plays a crucial role in enhancing image details(Attard et al., 2018). As illustrated in Fig.7., the DIs generated with CLAHE processing (b and e) and without (a and d) exhibit significant differences in the visibility of changes, as indicated by the red rectangles. Without CLAHE processing, some correct changes are compressed, making them difficult to discern. In contrast, the DI generated with CLAHE processing reveals hidden patterns in the raw images, as indicated by the contrast between the blue and green histograms in Fig. 7. (c) and (f). This is because CLAHE extends the raw pixel values to a larger range, making concealed patterns more discernible.
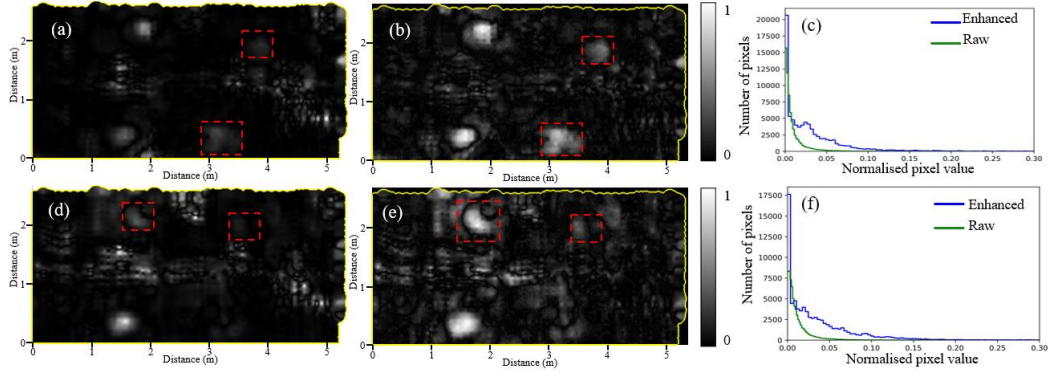
Fig. 7. Example of the CLAHE image enhancement function for small intensity differences in DI. (a) and (d) are raw DI, (b) and (e) are enhanced DI, and (c) and (f) are histograms of C-scans. Red rectangles indicate the relatively small intensity change in raw and enhanced DI.

In terms of noise resistance, two major types of noise are present in our task: local noise and noise clusters. Local noise, characterized by high pixel values and random distribution, is effectively diminished after the superpixel segmentation module. In this module, each superpixel is assigned the mean value of the pixels within it. Averaged by neighborhoods, superpixels containing local noise are less likely to be classified as changed areas in the subsequent FCM clustering and MRF classification. For instance, pixel-based DI and superpixel-based DI generated by methods (a) and (b) in Fig.8., respectively, demonstrate that some local noise (within the red rectangles) remaining in the pixel-based DI is eliminated through superpixel segmentation (shown in red rectangles in the panel). The other type of noise is cluster noise derived from the multiple representations of unchanged objects. In DI generation, the same targets in different C-scans sometimes remain incompletely eliminated, leaving some blocks at their edges, as shown by the white rectangles in (c), the superpixel-based DI created by (a) and (b) in Fig. 9. The MRF module also plays an essential role in creating resistance to this kind of noise. The spatial component of MRF considers adjacent neighborhoods of superpixels. For cluster noise in the superpixel-based DI, if there are no similar clusters in an adjacent field, the likelihood of classification as a changing area will decrease in the MRF model. It is unlikely that noise will cluster and repeat at the same location shown in C-scans at different depths. For example, Fig.9. (c) shows clustering noise with white rectangles, and there are no similar patterns in the adjacent C-scan (d). According to the energy function of MRF, these superpixels will usually be weighted as unchanged.
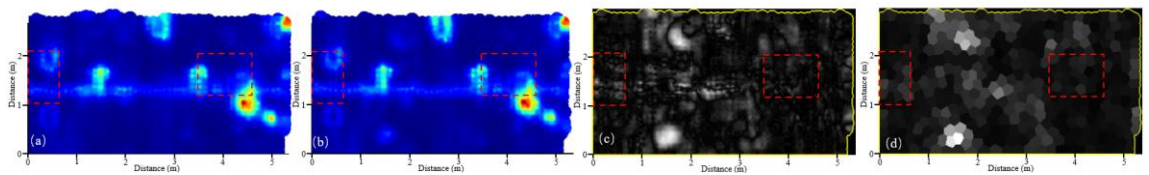

Fig.8. illustration of superpixel segmentation module for local noise resistance. (a) and (b) C-scans with and without targets. (c) pixel-based DI, (d) superpixel-based DI
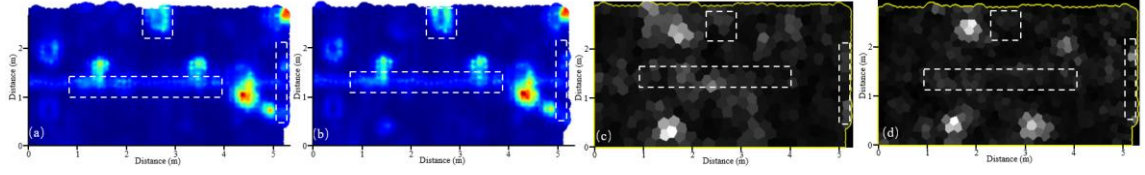
Fig. 9. Illustration of MRF module for noise cluster resistance. (a) and (b) C-scans with and without targets. (c) superpixel-based DI, (d) adjacent superpixel-based DI of (c)

Balancing image details and noise is integral in our proposed method. Equally important is the balance between the spatial and spectral components. The MRF model integrates these two types of information for change detection. In this experiment, we kept all other parameters fixed and varied only the value of β in equation (8), to record the F1-score achieved by different values of β. Fig. 10. shows the F1-scores for the four scenarios. When the parameter β is set to 0, the spatial component does not influence the energy function of the MRF, leading to subpar performance across all four scenarios, particularly the last three. As β increases from 0 to 4, all scenarios exhibit an increase in the F1-score, underscoring the beneficial impact of the spatial component. However, once β surpasses approximately 4, the F1-score begins to decline across all scenarios, in Fig.10. Interestingly, Scenario A consistently outperforms the other scenarios in terms of the F1-score, irrespective of the β value. This suggests that the MRF's contribution is less significant in Scenario A, and that the spectral component alone can yield satisfactory results. This is inherent to the nature of Scenario A, where all targets are centred within a single C-scan, thus enabling a single C-scan to capture all changes. Consequently, the spatial component's contribution is minimized in this scenario. Nonetheless, even with this minimized contribution, the F1-score still improves by 10% due to the spatial component. Based on our results, we selected β equals 4 as the optimal value, achieving the best balance between the spatial and spectral components in our method.
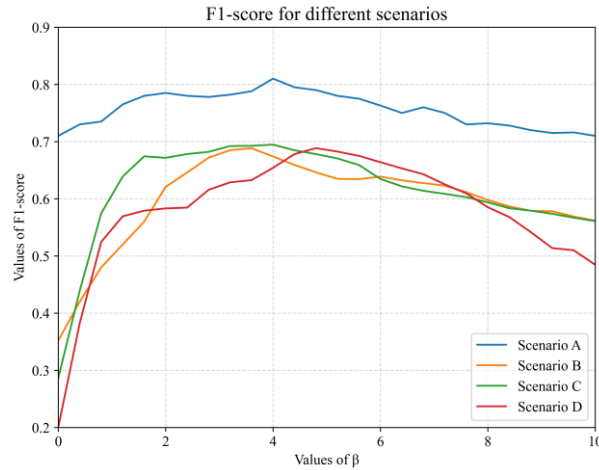

Fig.10. Influence of parameter β associated with four Scenarios.

B. Change Map Created Using the Proposed Method

Fig.11. demonstrates the effectiveness of the proposed method in detecting changes in the subsurface environment. The first and second columns of Fig.11. present the C-scans for the no-void cases and void cases in the four scenarios, respectively. Buried objects, such as continuous pipes and

manholes, can be identified in these normalized amplitude images. The third column displays the change maps generated by the proposed method using the pair of C-scans in the first two columns. The red circles in the change maps indicate the actual positions of the buried targets, and the white shapes represent the areas of change detected by the proposed method, with black areas indicating no change. As shown in Fig. 11., the proposed method successfully extracted the main body of the buried targets in all four scenarios, although the detected changed regions did not fully align with the ground truth. The proposed method achieved a 100% detection rate at the decision level, and the assessment metrics (TP, TN, FP, FN, F1-score, and kappa coefficient) calculated at the pixel level are summarized in Table 2. The F1-score (0.8, 0.69, 0.69, and 0.65) and kappa coefficient (0.79, 0.69, 0.68, and 0.64) demonstrate the robust performance of this method. Analysis of the detection results revealed that the F1-score and kappa coefficient for scenario A were relatively higher than those for the other three scenarios at the pixel level. This can be attributed to the relatively shallower depth of the buried balls with two shallow voids, which resulted in a relatively simple background. As the depth increased, the signal was increasingly affected, leading to increased noise in the C-scans. These factors likely contributed to the observed differences in performance across scenarios. In the following section, we discuss in more detail how the sub-modules contribute to the superior performance of the proposed method.
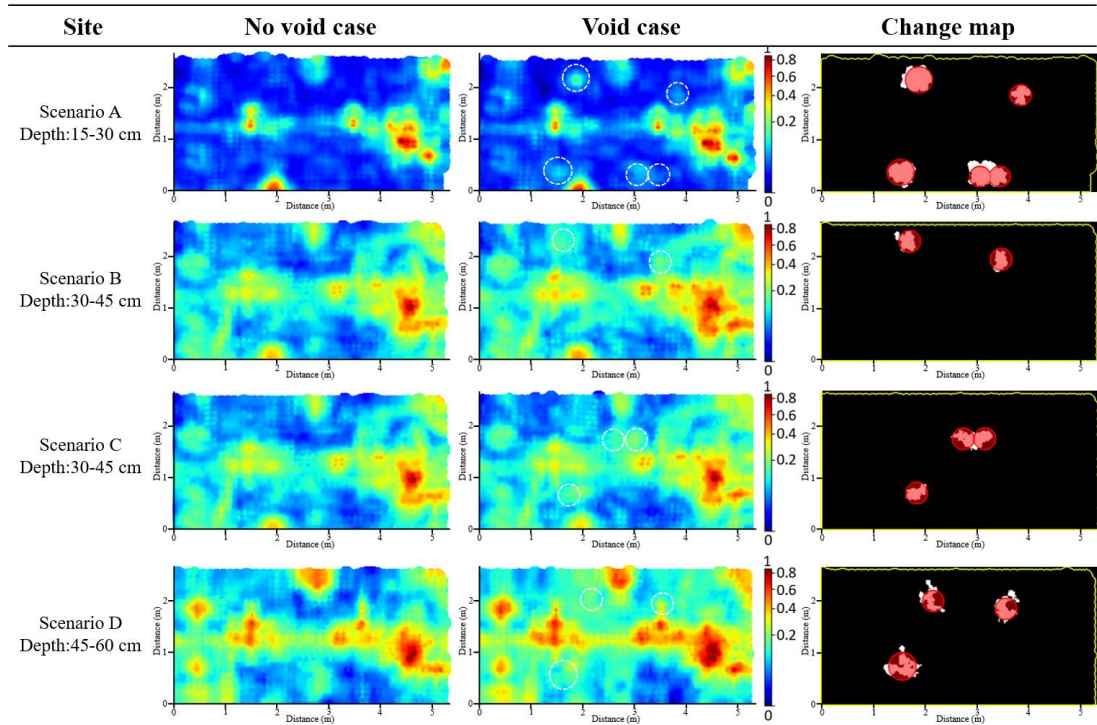
Fig. 11. Pairs of C-scans (no void case and void case) and change maps created using the proposed method with corresponding references in the four scenarios. (White regions are detected as changed areas and red masks refer to ground truth in change maps)

Table 2

TP, TN, FP, FN, F1-score, and Kappa Coefficient in the Four Scenarios

| Dataset	TP	TN	FN	FP	F1-score	Kappa coefficient
Scenario A	3145	62827	699	640	0.82	0.81
Scenario B	702	61730	524	99	0.69	0.69
Scenario C	1012	61136	826	94	0.69	0.68
Scenario D	1347	60305	888	574	0.65	0.64

D. Comparisons of different methods

To assess the impact of the proposed method on the results of C-scan change detection, we performed a comparison among different methods. Due to the absence of prior studies using the same data resources, we designed the comparison using different combinations of sub-modules of our method. The findings are presented in Fig. 12.-15. and Table 3, which depict the outcomes obtained by four different techniques for all scenarios. Fig. 12.-15. (a) shows the change map generated by the FCM+MRF (pixel-based) method. When compared with other subplots, the pixel-based method consistently produces scattered local false alarms through all four scenarios. In contrast, the superpixel-based method produces clusters that resist the effect of local noise, thereby emphasizing the contribution of superpixel segmentation in enhancing local noise resistance. Fig. 12.-15. (b) demonstrates the effectiveness of the MRF filter in eliminating noise clusters by integrating information along adjacent C-scans, particularly in scenarios B, C, and D. The change maps generated by the FCM+MRF-1 (superpixel-based) and FCM+MRF-2 (superpixel-based) methods, shown in Fig. 12.-15. (c) and (d), respectively, illustrate the significance of selecting the appropriate scale for the multi-scale strategy. FCM+MRF-1 uses the largest superpixels, while FCM+MRF-2 uses the smallest superpixels. Fig. 12. -15. (c) and (d) illustrate the contribution of the multi-scale decision fusion, where coarse superpixels can miss detection in scenario A and scenario B, and fine superpixels can result in cluster noise in scenario C. However, we observed less improvement in some scenarios when comparing the FCM and K-means methods. The primary distinction between these methods is that Fuzzy C-Means (FCM) employs a probability-based approach, as opposed to hard labeling, to characterize each pixel, as discussed in the methodology section. This variance confers an advantage to the overall method when the interpretation of the signal involves uncertainty, particularly in detecting comparatively deep changes. Consequently, while there is a relatively lower improvement observed in shallow scenario A, an increased improvement is observed in other scenarios. Our proposed method achieved the highest F-score and kappa coefficient compared to all other methods, indicating its superior performance. The comparison results also highlight the contribution of each sub-module in our proposed method.
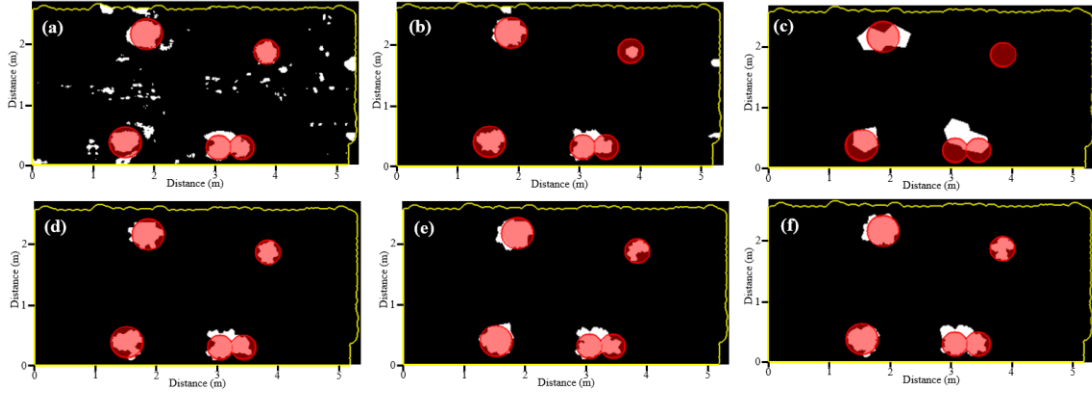
Fig. 12. Change maps generated by different methods in scenario A. (a) FCM +MRF (pixel-based). (b) FCM + Multiscale decision fusion (superpixel-based). (c) FCM +MRF-1 (superpixel-based). (d) FCM +MRF-2 (superpixel-based). (e) K-means + MRF + Multiscale decision fusion (superpixel-based). (f) FCM + MRF + Multiscale decision fusion (superpixel-based)
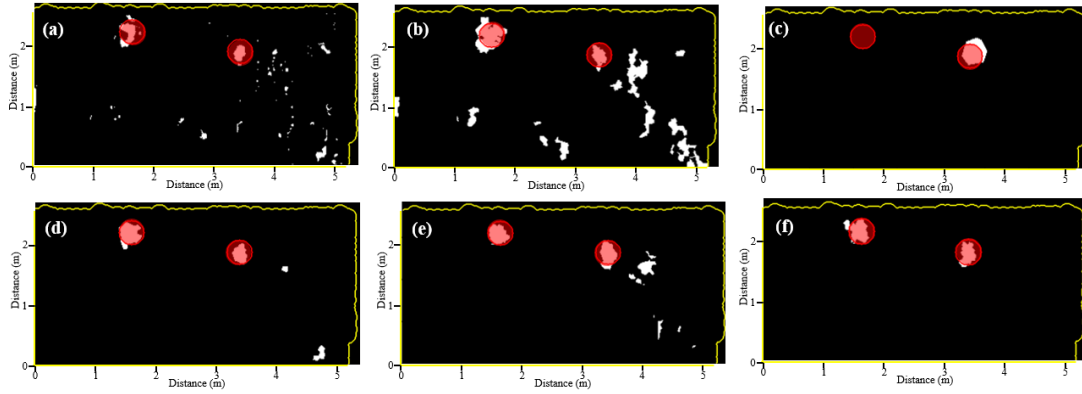
Fig. 13. Change maps generated by different methods in scenario B. (a) FCM +MRF (pixel-based). (b) FCM + Multiscale decision fusion (superpixel-based). (c) FCM +MRF-1 (superpixel-based). (d) FCM +MRF-2 (superpixel-based). (e) K-means + MRF + Multiscale decision fusion (superpixel-based). (f) FCM + MRF + Multiscale decision fusion (superpixel-based)
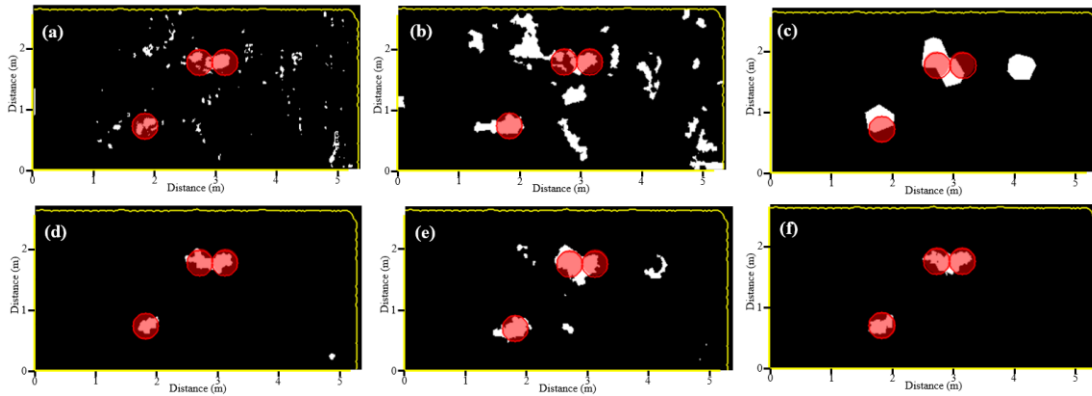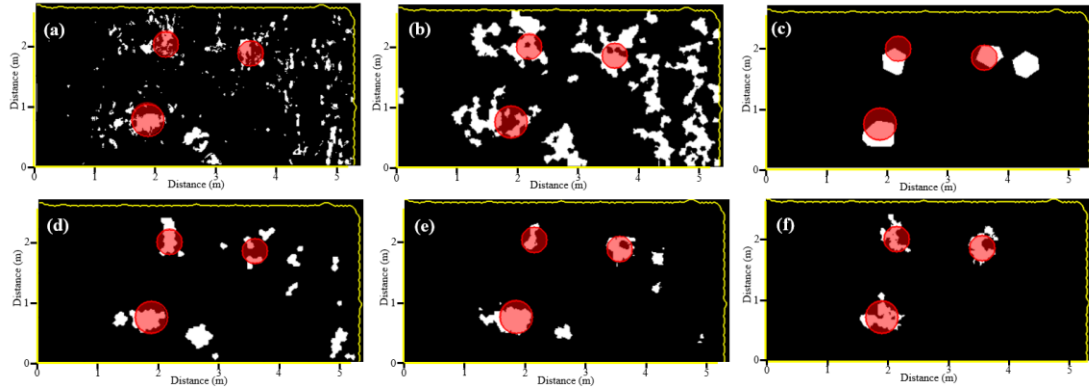

Fig. 14. Change maps generated by different methods in scenario C. (a) FCM +MRF (pixel-based). (b) FCM + Multiscale decision fusion (superpixel-based). (c) FCM +MRF-1 (superpixel-based). (d)

FCM +MRF-2 (superpixel-based). (e) K-means + MRF + Multiscale decision fusion (superpixel-based). (f) FCM + MRF + Multiscale decision fusion (superpixel-based)

Fig. 15. Change maps generated by different methods in scenario D. (a) FCM +MRF (pixel-based). (b) FCM + Multiscale decision fusion (superpixel-based). (c) FCM +MRF-1 (superpixel-based). (d) FCM +MRF-2 (superpixel-based). (e) K-means + MRF + Multiscale decision fusion (superpixel-based). (f) FCM + MRF + Multiscale decision fusion (superpixel-based)

Table 3 Comparison of the change detection results obtained by different methods

Methods	Scenario A		Scenario B		Scenario C		Scenario D	
	F1-score	Kappa coefficient	F1-score	Kappa coefficient	F1-score	Kappa coefficient	F1-score	Kappa coefficient
FCM +MRF (pixel-based)	0.63	0.61	0.38	0.37	0.39	0.38	0.29	0.26
FCM+ Multiscale decision fusion (superpixel-based)	0.71	0.70	0.35	0.33	0.28	0.25	0.20	0.15
FCM+MRF-1 (superpixel-based)	0.48	0.51	0.45	0.45	0.44	0.42	0.46	0.44
FCM+MRF-2 (superpixel-based)	0.79	0.78	0.68	0.67	0.63	0.62	0.39	0.37
K-means + MRF + Multiscale	0.80	0.80	0.63	0.62	0.65	0.64	0.62	0.61
FCM + MRF + Multiscale decision fusion (superpixel-based)	**0.82**	**0.81**	**0.69**	**0.69**	**0.69**	**0.68**	**0.65**	**0.64**

5. Conclusion

This paper presents a novel unsupervised change detection method for subsurface imaging using GPR time-lapse images. The method utilizes a combination of standard processing functions, image registration, superpixel-based DI generation, and image classification via fuzzy C-means and Markov random field method. The proposed method offers three key innovations: first, a clustering algorithm is applied to generate multiscale superpixels, which enhances local noise resistance and reduces the chances of mis- or over-detection due to inappropriate scale selection. Second, a fuzzy C-means clustering algorithm is used to classify the superpixel-based DI, which uses fuzzy membership to represent the relationships between different superpixels instead of hard labels. Finally, the MRF method is employed to integrate vertical information by considering the spatial component, which compensates for the fact that single-slice change detection typically focuses only on horizontal patterns and ignores vertical connectivity. The proposed method was tested in four scenarios, and the results indicate high performance and reliability as evidenced by F1-scores (ranging from 0.65, 0.69,0.69 and 0.82) and kappa coefficients (ranging from 0.64, 0.68, 0.69,0.81). However, there are acknowledged limitations to this study. Specifically, the lack of regular field data to further test the robustness of the method, and the targets and test site upscaled from a practical case. In conclusion, the proposed unsupervised superpixel-based change detection method offers substantial potential for detecting subsurface changes in GPR time-lapse images. Further testing and refinement will be necessary to address the limitations of the current study and fully evaluate the effectiveness of this method for real-world applications.

Declaration of interests

The authors declare that they have no known competing financial interests or personal relationships that could have appeared to influence the work reported in this paper.

Reference

Achanta, R., Shaji, A., Smith, K., Lucchi, A., Fua, P., & Süsstrunk, S. (2012). SLIC Superpixels Compared to State-of-the-Art Superpixel Methods. *IEEE Transactions on Pattern Analysis and Machine Intelligence*, *34*(11), 2274–2282. https://doi.org/10.1109/TPAMI.2012.120

Annan, A. P. (2004). Ground penetrating radar applications, principles, procedures. *Mississauga, Canada: Sensors and Software*.

Attard, L., Debono, C. J., Valentino, G., & Di Castro, M. (2018). Vision-based change detection for inspection of tunnel liners. *Automation in Construction*, *91*, 142–154. https://doi.org/10.1016/j.autcon.2018.03.020

Bezdek, J. C. (1984). FCM: THE FUZZY c-MEANS CLUSTERING ALGORITHM. In *Computers & Geosciences* (Vol. 10, Issue 3).

Broere, W. (2016). Urban underground space: Solving the problems of today's cities. *Tunnelling and Underground Space Technology*, *55*, 245–248. https://doi.org/https://doi.org/10.1016/j.tust.2015.11.012

Chi, Y. M., Mallik, U., Clapp, M. A., Choi, E., Cauwenberghs, G., & Etienne-Cummings, R. (2007). CMOS Camera With In-Pixel Temporal Change Detection and ADC. *IEEE Journal of Solid-State Circuits*, *42*(10), 2187–2196. https://doi.org/10.1109/JSSC.2007.905295

Desclée, B., Bogaert, P., & Defourny, P. (2006). Forest change detection by statistical object-based method. *Remote Sensing of Environment*, *102*(1), 1–11. https://doi.org/https://doi.org/10.1016/j.rse.2006.01.013

El-Mahallawy, M. S., & Hashim, M. (2013). Material Classification of Underground Utilities From GPR Images Using DCT-Based SVM Approach. *IEEE Geoscience and Remote Sensing Letters*, *10*(6), 1542–1546. https://doi.org/10.1109/LGRS.2013.2261796

Feng, J., Yang, L., Wang, H., Tian, Y., & Xiao, J. (n.d.). *Subsurface Pipes Detection Using DNN-based Back Projection on GPR Data*.

Goodman, D. (2004). Gpr-slice. ground penetrating radar imaging software. user's manual. *Geophysical Archaeometry Laboratory, California*.

Hussain, M., Chen, D., Cheng, A., Wei, H., & Stanley, D. (2013). Change detection from remotely sensed images: From pixel-based to object-based approaches. In *ISPRS Journal of Photogrammetry and Remote Sensing* (Vol. 80, pp. 91–106). Elsevier B.V. https://doi.org/10.1016/j.isprsjprs.2013.03.006

Inglacla, J., & Mercier, G. (2007). A new statistical similarity measure for change detection in multitemporal SAR images and its extension to multiscale change analysis. *IEEE Transactions on Geoscience and Remote Sensing*, *45*(5), 1432–1445. https://doi.org/10.1109/TGRS.2007.893568

Jol, H. M. (2008). *Ground Penetrating Radar Theory and Applications*. Oxford: Elsevier Science & Technology.

Joll, H. M. (2009). *Ground penetrating radar theory and applications*.

Li, M. D., Chang, K., Bearce, B., Chang, C. Y., Huang, A. J., Campbell, J. P., Brown, J. M., Singh, P., Hoebel, K. v., Erdoğmuş, D., Ioannidis, S., Palmer, W. E., Chiang, M. F., & Kalpathy-Cramer, J. (2020). Siamese neural networks for continuous disease severity evaluation and change detection in medical imaging. *Npj Digital Medicine*, *3*(1), 1–9. https://doi.org/10.1038/s41746-020-0255-1

Lowekamp, B. C., Chen, D. T., Ibáñez, L., & Blezek, D. (2013). The design of simpleITK. *Frontiers in Neuroinformatics*, *7*(DEC). https://doi.org/10.3389/fninf.2013.00045

Lu, D., Mausel, P., Brondízio, E., & Moran, E. (2004). Change detection techniques. *International Journal of Remote Sensing*, *25*(12), 2365–2401. https://doi.org/10.1080/0143116031000139863

Luo, T. X. H., & Lai, W. W. L. (2020a). GPR pattern recognition of shallow subsurface air voids. *Tunnelling and Underground Space Technology*, *99*(February), 103355. https://doi.org/10.1016/j.tust.2020.103355

Luo, T. X. H., & Lai, W. W. L. (2020b). Subsurface Diagnosis with Time-Lapse GPR Slices and Change Detection Algorithms. *IEEE Journal of Selected Topics in Applied Earth Observations and Remote Sensing*, *13*, 935–940. https://doi.org/10.1109/JSTARS.2020.2975659

Luo, T. X. H., Lai, W. W. L., Chang, R. K. W., & Goodman, D. (2019). An empirical study of GPR imaging criteria. *Journal of Applied Geophysics*, *165*, 37–48. https://doi.org/10.1016/j.jappgeo.2019.04.008

Lv, N., Chen, C., Qiu, T., & Sangaiah, A. K. (2018). Deep Learning and Superpixel Feature Extraction Based on Contractive Autoencoder for Change Detection in SAR Images. *IEEE Transactions on Industrial Informatics*, *14*(12), 5530–5538. https://doi.org/10.1109/TII.2018.2873492

Milisavljeviã, N., Bloch, I., van den Broek, S., & Acheroy, M. (2003). Improving mine recognition through processing and Dempster-Shafer fusion of ground-penetrating radar data. In *Pattern Recognition* (Vol. 36). www.elsevier.com/locate/patcog

Rensink, R. A. (2002). Change Detection. *Annual Review of Psychology*, *53*(1), 245–277. https://doi.org/10.1146/annurev.psych.53.100901.135125

Reza, A. M. (2004). Realization of the Contrast Limited Adaptive Histogram Equalization (CLAHE) for Real-Time Image Enhancement. *Journal of VLSI Signal Processing Systems for Signal, Image and Video Technology*, *38*(1), 35–44. https://doi.org/10.1023/B:VLSI.0000028532.53893.82

Rokni, K., Ahmad, A., Solaimani, K., & Hazini, S. (2015). A new approach for surface water change detection: Integration of pixel level image fusion and image classification techniques. *International Journal of Applied Earth Observation and Geoinformation*, *34*, 226–234. https://doi.org/https://doi.org/10.1016/j.jag.2014.08.014

Seo, J., Park, W., & Kim, T. (2022). Feature-Based Approach to Change Detection of Small Objects from High-Resolution Satellite Images. *Remote Sensing*, *14*(3), 462.

Simanjuntak, R. M., Kuffer, M., & Reckien, D. (2019). Object-based image analysis to map local climate zones: The case of Bandung, Indonesia. *Applied Geography*, *106*(April), 108–121. https://doi.org/10.1016/j.apgeog.2019.04.001

Stow, D. A. (1999). Reducing the effects of misregistration on pixel-level change detection. *International Journal of Remote Sensing*, *20*(12), 2477–2483. https://doi.org/10.1080/014311699212137

Walter, V. (2004). Object-based classification of remote sensing data for change detection. *ISPRS Journal of Photogrammetry and Remote Sensing*, *58*(3–4), 225–238.

Zhang, M., & Shi, W. (2020). A Feature Difference Convolutional Neural Network-Based Change Detection Method. *IEEE Transactions on Geoscience and Remote Sensing*, *58*(10), 7232–7246. https://doi.org/10.1109/TGRS.2020.2981051

Zhu, X., & Liu, D. (2014). MAP-MRF approach to landsat ETM+ SLC-Off image classification. *IEEE Transactions on Geoscience and Remote Sensing*, *52*(2), 1131–1141. https://doi.org/10.1109/TGRS.2013.2247612